Interfacial debonding detection of strengthened steel structures by using smart CFRP-FBG composites

Hua-Ping Wang[1,2,3], Yi-Qing Ni[2,3,*], Jian-Guo Dai[2] and Mao-Dan Yuan[4]

[1]School of Civil Engineering and Mechanics, Lanzhou University, Lanzhou 730000, China
Email: wanghuaping1128@sina.cn; hpwang@lzu.edu.cn

[2]Department of Civil and Environmental Engineering, The Hong Kong Polytechnic University, Hung Hom, Kowloon, Hong Kong

[3]Hong Kong Branch of National Rail Transit Electrification and Automation Engineering Technology Research Centre, The Hong Kong Polytechnic University, Hung Hom, Kowloon, Hong Kong

[4]Department of Electromechanical Engineering, Guangzhou University of Technology, Guangzhou 510006, China

~~[5]Department of Systems Engineering and Engineering Management, City University of Hong Kong, Hong Kong~~

Corresponding author: yiqing.ni@polyu.edu.hk (Y.Q. Ni)

Abstract: The interfacial debonding detection of multi-layered strengthened structures (i.e., carbon fiber reinforced polymer (CFRP) strengthened steel/concrete beams) has always been an important issue related to the integrity of this kind of composite structures. Direct use of fiber Bragg grating (FBG) sensors is difficult to perceive the shear strain. With the intention of accurately monitoring the interfacial bonding state based on optical fiber sensing technology, a smart CFRP-FBG composite is developed in this study. A theoretical model of the strengthened steel beam is first formulated to relate the interfacial shear stress with the normal stress of the CFRP-FBG composites. After confirming the structural integrity of the composites by an ultrasonic nondestructive testing technique, loading tests are conducted to examine the measurement accuracy of the FBGs embedded in series and the effectiveness of the composites in detecting the interfacial debonding failure. Results indicate that the proposed smart CFRP-FBG composites can accurately identify the interfacial debonding of the multi-layered structures, and the degradation process of the interfacial bonding state can be favorably reflected by the variation of strain profiles measured by the FBGs embedded in series in the composites. The developed CFRP-FBG composites can be adopted to identify the damage and facilitate in-time maintenance of the multi-layered structures in practical applications.

Keywords: Smart CFRP-FBG composites, strengthened steel structures, interfacial debonding, shear stress, structural health monitoring

1. Introduction

Civil structures are always in the process of successive deterioration , due to the loading and environmental effects, natural and man-made disasters, and quality-control defects [1-3]. To undermine the deteriorating process and extend the service life of aging and degraded structures, strengthening and rehabilitating techniques become both environmentally and economically preferable rather than replacements. One of the widely accepted methods is the use of externally

bonded carbon fiber reinforced polymer (CFRP) composites on the tensile surface of girder structures. Because of high strength, good durability, corrosion resistance and light weight of the composite materials, the flexural and shear performance and load-carrying capacity of the reinforced structures can be improved [4-5]. It is a competitive alternative to the conventional strengthening methods by using steel and concrete materials [6]. Although CFRP reinforced structures become more and more prevalent, the design method, damage and failure mechanisms, and durability are yet to be fully investigated.

Research attempts including experimental studies, numerical analysis and theoretical exploration have been made to understand the mechanical behavior of CFRP strengthened concrete and steel structures [7-15]. The interfacial bonding state between the CFRP composite and the substrate structure is the utmost importance, because the gradual interfacial degradation leads to the premature debonding that greatly decreases the reinforcing effect [16-20]. In recent years, efforts have been given on developing structurally effective adhesives to prevent the debonding. However, the interfacial debonding is still the universal failure mode of CFRP reinforced structures [21]. With the failure of reinforcing measure, the deficient concrete/steel girder structures may fall down in a brittle manner under the double effect of heavy traffic load and extreme service environment, which can induce tremendous economic loss and even casualties. However, if the interfacial debonding can be accurately detected and the rehabilitation can be conducted in time, the unfavorable effect mentioned above can be alleviated [22-25]. Therefore, the condition monitoring of interfacial bonding state is critically important.

Besides the interfacial bonding state, the reinforcing effect is also a significant aspect that structural engineers care. Researchers have explored the reinforcing effect by comparing the mechanical performance of reinforced structure with that of the unreinforced one [17, 26-30], which is feasible for laboratory experimental study. In practical engineering, the reinforcing measure is often projected according to the reinforcing design code that is largely based on the findings from laboratory tests. However, the differences on scale size, construction and loading environment of the structure in field with that in laboratory may lead to the actual reinforcing effect weaker than the design expectation. It is also worth noting that the enhancement of strength and stiffness can be guaranteed only when a satisfactory bonding state between the host structure and the attached CFRP composite is maintained.

The interfacial bonding state usually experiences a gradual and invisible degradation process before the debonding can be straightforwardly observed. The unseen damage growing to critical levels without detection is a serious cause for concern. Sensing techniques by using strain gauges [19,31-32], acoustic emission [33], piezoceramics [34], ultrasonic wave [35-37] and infrared imaging [38-39] have been applied to detect the debonding, but with significant limitations. For example, they

have shown high susceptibility to electromagnetic interference of vehicles in motion, and are difficult to monitor the occurrence and propagation of damage with high precision [40]. To overcome these shortcomings, advanced optical fiber sensing technologies with characteristics of high sensitivity and precision, long-term stability and durability, good geometrical shape-versatility, corrosion resistance, anti-electromagnetic interference and low cost have been adopted [41-43]. Furthermore, due to the narrow-band wavelength reflection, FBGs are conveniently multiplexed in a sensing network by using wavelength-domain multiplexing technique [44-50].

Surface-attached FBGs can be used to directly measure the strain of CFRP composite and the reinforced structure. In this regard, the function of FBGs is similar to strain gauges. The change of interfacial bonding state can be roughly detected by embedding optical fiber sensors into the adhesive layer [51-52]. However, to make full use of FBGs and conveniently realize the strain monitoring, FBGs can be integrated with CFRP composites to configure the smart CFRP-FBG composites. Previous studies focused on exploring the mechanical behavior and possible damage modes (i.e., crack and delamination) of the CFRP composite embedded with bare FBGs under different loading conditions (i.e., impact and fatigue loads) [53-55]. Some research presented preliminary investigations on the possible application of the smart CFRP strips embedded with FBGs and distributed optical fibers for strengthening and monitoring the structures [56-61]. However, these studies emphasize the performance of the CFRP composites, and ignore the potential application of the smart composites.

Given the above, smart CFRP-FBG composites are proposed in this study to simultaneously strengthen the structure and monitor the interfacial debonding. The uniqueness of this technique is the in-situ self-sensing of damage, which is in parallel with the development of nondestructive testing and evaluation techniques. CFRP material is adopted to package FBGs and configure the smart CFRP-FBG composites. The smart CFRP-FBG composite can be regarded as a novel sensor, which can not only realize the monitoring function, but also offer the strengthening function. A theoretical study is presented to demonstrate the feasibility of the proposed method, and experimental verification is performed to validate the effectiveness.

2. Theoretical modeling and analysis

2.1 Model description

To monitor the interfacial debonding of a CFRP reinforced structure, it is essential to understand the mutual interaction and the damage mechanism. Therefore, a theoretical model is first formulated to describe the stress relationships. A steel beam model with a H-shaped cross section is considered, where a CFRP composite is attached on the beam bottom. As shown in Fig. 1, the simply supported constraint and four-point bending loading are considered. The span and the height of the beam are $2(l+a)$ and $2z_0$, respectively. The length, width and thickness of the CFRP composite are separately

denoted as $2l$, b_c and t_c. P is the load. b is the distance of the load point to the origin of the coordinate. The origin of the coordinate system is located at the neutral axis of the beam.

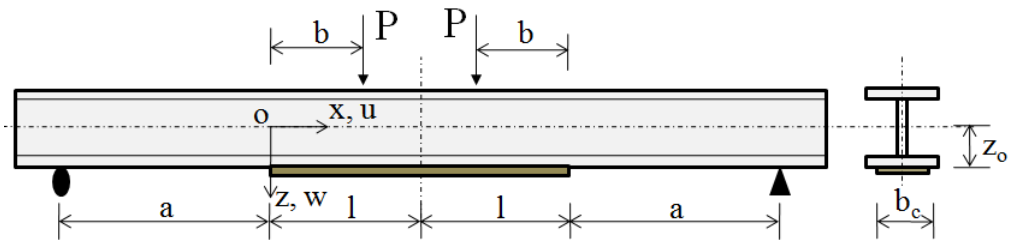

Fig. 1 Steel beam strengthened with CFRP composite

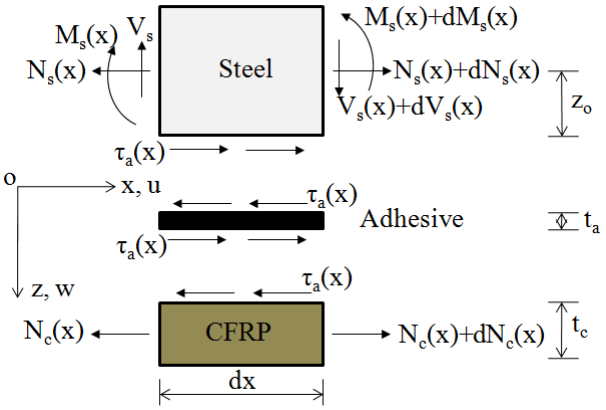

Fig. 2 Infinitesimal element of a three-layered strengthened beam

To obtain a general expression, an arbitrary cross section is considered in the theoretical derivation. An infinitesimal element, dx, is selected from the reinforced beam. The stress state of a three-layered model is shown in Fig. 2. $M_s(x)$, $N_s(x)$ and $V_s(x)$ are the bending moment, axial force and shear force of the steel beam, respectively. $N_c(x)$ is the axial force of the CFRP composite. $\tau_a(x)$ is the interfacial shear stress. The thickness of the adhesive layer is t_a. Two assumptions are made hereafter: (i) the bending stiffness of the beam to be strengthened is much greater than the stiffness of the strengthening plate; and (ii) the stresses in the adhesive layer don't change along the thickness direction (i.e., the adhesive layer is thin). Therefore, the bending moment in the CFRP composite is negligible, which implies that the normal stress in the bonding zone can be ignored, as displayed in Fig. 2.

2.2 Theoretical analysis

The applied load can be transferred to the CFRP composite by the interfacial stresses between the steel and the adhesive, and the adhesive and the CFRP composite. The compatibility condition of the three-layered beam structure produces the shear stress in the adhesive layer as [12]:

$$\tau_a(x) = \frac{G_a}{t_a}[u_c(x) - u_s(x)] \tag{1}$$

where $u_c(x)$ and $u_s(x)$ are separately the displacements of the CFRP composite and the steel beam along the x-direction; G_a is the shear modulus of the adhesive.

The strains of the steel beam and the CFRP composite can be given by the following equations [29]:

$$\varepsilon_s(x)=\frac{du_s(x)}{dx}=\frac{M_s(x)}{E_sW_s}-\frac{N_s(x)}{E_sA_s};\ \varepsilon_c(x)=\frac{du_c(x)}{dx}=\frac{N_c(x)}{E_cA_c} \tag{2}$$

where E_s, W_s and A_s are the elastic modulus, section modulus in bending and cross-sectional area of the steel beam, respectively; E_c and A_c are the elastic modulus and cross-sectional area of the CFRP composite.

Differentiating Eq. (1) and Eq. (2) with respect to x yields:

$$\frac{d^2\tau_a(x)}{dx^2}=\frac{G_a}{t_a}[\frac{d^2u_c(x)}{dx^2}-\frac{d^2u_s(x)}{dx^2}] \tag{3}$$

$$\frac{d^2u_s(x)}{dx^2}=\frac{1}{E_sW_s}\frac{dM_s(x)}{dx}-\frac{1}{E_sA_s}\frac{dN_s(x)}{dx} \tag{4}$$

$$\frac{d^2u_c(x)}{dx^2}=\frac{1}{E_cA_c}\frac{dN_c(x)}{dx} \tag{5}$$

where

$$\frac{dM_s(x)}{dx}=V_s(x)-\tau_a(x)b_cz_o=P-\tau_a(x)b_cz_o \tag{6}$$

$$\frac{dN_s(x)}{dx}=\tau_a(x)b_c;\ \frac{dN_c(x)}{dx}=\tau_a(x)b_c \tag{7}$$

Substituting Eqs. (6) and (7) into Eqs. (4) and (5) generates:

$$\frac{d^2u_s(x)}{dx^2}=\frac{1}{E_sW_s}[P-\tau_a(x)b_cz_o]-\frac{\tau_a(x)b_c}{E_sA_s}=\frac{p}{E_sW_s}-(\frac{b_cz_o}{E_sW_s}+\frac{b_c}{E_sA_s})\tau_a(x) \tag{8}$$

$$\frac{d^2u_c(x)}{dx^2}=\frac{1}{E_cA_c}\tau_a(x)b_c \tag{9}$$

and then substituting Eqs. (8) and (9) into Eq. (3) yields:

$$\frac{d^2\tau_a(x)}{dx^2}=\frac{G_a}{t_a}[(\frac{b_c}{E_cA_c}+\frac{b_cz_o}{E_sW_s}+\frac{b_c}{E_sA_s})\tau_a(x)-\frac{P}{E_sW_s}] \tag{10}$$

Thus the governing equation can be rewritten as

$$\frac{d^2\tau_a(x)}{dx^2}-\lambda^2\tau_a(x)+\frac{G_a}{E_sW_st_a}P=0 \tag{11}$$

where $\lambda^2=\frac{G_ab_c}{t_a}(\frac{1}{E_cA_c}+\frac{z_o}{E_sW_s}+\frac{1}{E_sA_s})$.

The solution of Eq. (11) and its first derivative with respect to x are given by

$$\tau_a(x)=C_1\cosh(\lambda x)+C_2\sinh(\lambda x)+\frac{G_a}{\lambda^2E_sW_st_a}P \tag{12}$$

$$\frac{d\tau_a(x)}{dx}=C_1\lambda\sinh(\lambda x)+C_2\lambda\cosh(\lambda x) \tag{13}$$

Since a singularity beneath the point load P exists, the differential equation (12) is valid for $0 < x < b$ [62]. Hence, the following formulas can be obtained from the constraints:

$$\tau_a(x)=0 \quad \text{at} \quad x=b \tag{14a}$$

$$N_s=N_c=0 \quad \text{at} \quad x=0 \tag{14b}$$

$$M_s=Pa \quad \text{at} \quad x=0 \tag{14c}$$

The subtraction of Eq. (1) from Eq. (2) yields:

$$\frac{d\tau_a(x)}{dx}=\frac{G_a}{t_a}\left[\frac{N_c(x)}{E_cA_c}-\frac{M_s(x)}{E_sW_s}+\frac{N_s(x)}{E_sA_s}\right] \tag{15}$$

If $x = 0$, it reduces to:

$$\frac{d\tau_a(x)}{dx}=-\frac{G_a}{t_a}\frac{M_s(x)}{E_sW_s}=-\frac{G_aPa}{t_aE_sW_s} \tag{16}$$

Making use of Eq. (16), the constant C_2 can be obtained from Eq. (13) as

$$C_2=-\frac{G_aPa}{\lambda t_aE_sW_s} \tag{17}$$

and the constant C_1 can be derived from Eq. (14a) as

$$C_1=\frac{G_aPa}{\lambda t_aE_sW_s}\frac{\sinh(\lambda b)}{\cosh(\lambda b)}-\frac{G_a}{\lambda^2E_sW_st_a}\frac{V_s(x)}{\cosh(\lambda b)} \tag{18}$$

The interfacial shear stress can be expressed as

$$\tau_a(x)=\frac{G_aP}{t_aE_sW_s}\left[\frac{a}{\lambda}\tanh(\lambda b)\cosh(\lambda x)-\frac{\cosh(\lambda x)}{\lambda^2\cosh(\lambda b)}-\frac{a}{\lambda}\sinh(\lambda x)+\frac{1}{\lambda^2}\right] \tag{19}$$

According to the assumption given in [62], if $\lambda b > 5$, Eq. (19) can be simplified as

$$\tau_a(x)=\frac{G_aP}{t_aE_sW_s}\frac{a\lambda e^{-\lambda x}+1}{\lambda^2} \tag{20}$$

By using Eq. (2) and Eq. (7), the normal stress of the CFRP composite can be obtained as

$$\sigma_c(x)=\frac{G_aP}{t_ct_aE_sW_s}\frac{a(1-e^{-\lambda x})+x}{\lambda^2},\ 0\le x\le b \tag{21}$$

A physical model to be tested in Section 4 is discussed here. The geometrical and material parameters of the steel beam and the CFRP composite are described in Table 1. The distribution of the interfacial shear stress and the normal stress of the CFRP composite under the load (P = 1 kN) can be obtained by substituting the given parameters into Eq. (20) and Eq. (21). The abscissa axis in Fig. 3 is x, with its value ranging from 0 to b. As shown in Fig. 3(a), the interfacial shear stress decreases nonlinearly from the end to the central and the maximum value occurs in the end (x=0). The normal stress of the CFRP composite presents an increasing tendency from the end to the central as shown in Fig. 3(b) and the maximum value is at the position adjacent to the central. Besides, the normal stress of the CFRP composite is far larger than the interfacial shear stress. In general, the interfacial shear stress can be reflected from the normal stress of the CFRP composite if the interface is in an ideal bonding state without damage or degradation.

Table 1 Physical parameters of the CFRP reinforced steel beam in test

Parameter	Label	Value	Unit
Flange thickness		9×10^{-3}	m
Web width		6×10^{-3}	m
Width		1.25×10^{-1}	m
Half of the height	z_0	6.25×10^{-2}	m
Area of cross section of steel beam	A_s	2.892×10^{-3}	m^2
Area of cross section of CFRP composite	A_c	3×10^{-4}	m^2
Width of CFRP composite	b_c	1×10^{-1}	m
Thickness of adhesive layer	t_a	1.5×10^{-3}	m
Young's modulus of steel	E_s	2.06×10^{11}	N/m^2
Young's modulus of CFRP	E_c	3.07×10^{11}	N/m^2
Shear modulus of adhesive	G_a	1.154×10^{9}	N/m^2

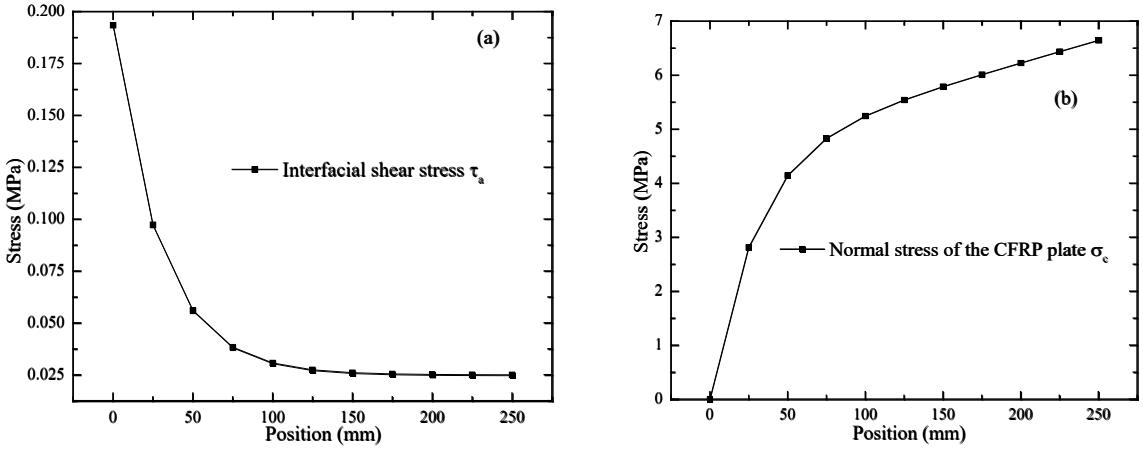

Fig. 3 Stress profiles under the load of P = 1 kN: (a) Interfacial shear stress; (b) Normal stress of the CFRP composite

3. Smart CFRP-FBG composite

3.1 Fabrication procedure

The smart CFRP-FBG composite embedded with quasi-distributed FBGs in series is developed to monitor the interfacial bonding state between the reinforced structure and the surface-attached CFRP composite. Vacuum hot-pressed sintered technology is adopted to mold the smart composite. The main equipment used in production is the econoclave (EC1.2 m × 2.4 m) with working diameter 1219 mm and working length 2438 mm. The maximum operating pressure is 150 psi. The cross section of the CFRP composite is 100 mm × 700 mm, and the thickness is 3 mm. A 3-mm-thickness plate is laminated by 16-layer carbon fiber strips and the thickness of each strip is 0.2 mm. The detailed fabrication process can be described as follows: (i) 16 pieces of CFRP strips are prepared and the cross section of each strip is about 150 mm × 750 mm,

slightly larger than the design size; (ii) 8 pieces of strips immersed in epoxy resin are piled up on the high strength aluminum alloy platform and then the FBGs in series are fixed on the 8-layer CFRP strips, as displayed in Fig. 4(a); (iii) The remaining 8 pieces of strips are paved by layers and the roller is employed to artificially compact the laminates, as shown in Fig. 4(b); (iv) Blue plastic films are placed on the surface of the CFRP laminates and the leading-out optical fiber lines. They are used to keep the epoxy resin from the white stone cotton. The vacuum compacting is then conducted to primarily cure the multi-layer laminates (see Fig. 4(c) and Fig. 4(d)). The process lasts about 3 hours; (v) Small aluminum samples are then placed on the cured CFRP laminates. Thermal couple probes are then fixed on the central and the side end to detect the curing temperature during the vacuum hot-pressed process in the econoclave (see Fig. 4(e) and Fig. 4(f)); and (vi) The sealed CFRP laminates are then placed into the econoclave and the vacuum pressurization process lasts about 3.5 hours. The pressure and temperature variations in the ASC (Autoclave Systems for Aerospace Composites) process system are provided in Fig. 5; and (vii) The molded CFRP composites are taken from the econoclave and smart CFRP-FBG composites are successfully achieved (see Fig. 4(g) and Fig. 4(h)). Two smart CFRP-FBG composites have been fabricated to examine the stability of the structural performance. One sample without FBGs has also been fabricated for tensile test.

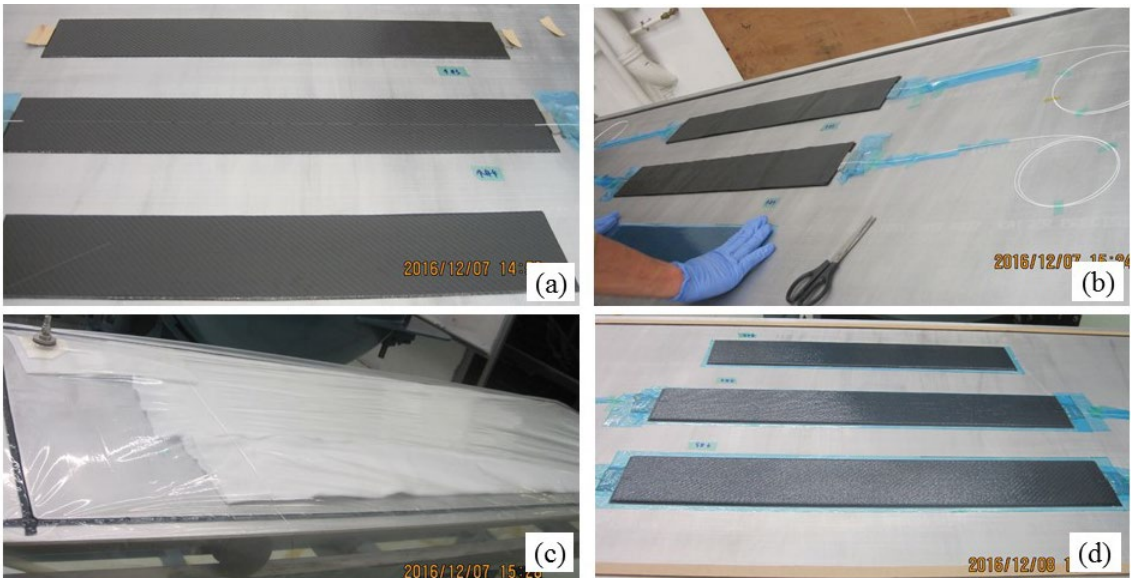

Fig. 4 Fabrication procedure of the smart CFRP-FBG composite: (a) FBGs in series fixed on the 8-layer CFRP strips; (b) 16-layer CFRP strips embedded with FBGs in series; (c) Seal for vacuum preloading; (d) Initial molding composite; (e) Installation of thermal couplers; (f) ASC process system; (g) Second molding composite; (h) CFRP-FBG composite

Optical fiber patch cords have been adopted to connect the leading-out fibers of the smart CFRP-FBG composites to the interrogator SM130 produced by Micro Optics Inc. The central wavelengths of FBGs in series in the CFRP composites are presented in Fig. 6. The signal check shows that the FBGs in series in the two composites perform well and a 100% survival ratio is achieved. It indicates that the smart CFRP-FBG composite can be successfully constructed by the proposed fabrication process and FBGs embedded in the CFRP composite can survive. Another important point is that the careful protection of the leading-out optical fibers at the two ends of the CFRP composite should be conducted to keep the brittle fiber from the immersion of epoxy resin and the possible shear force incurred in the fabrication process.

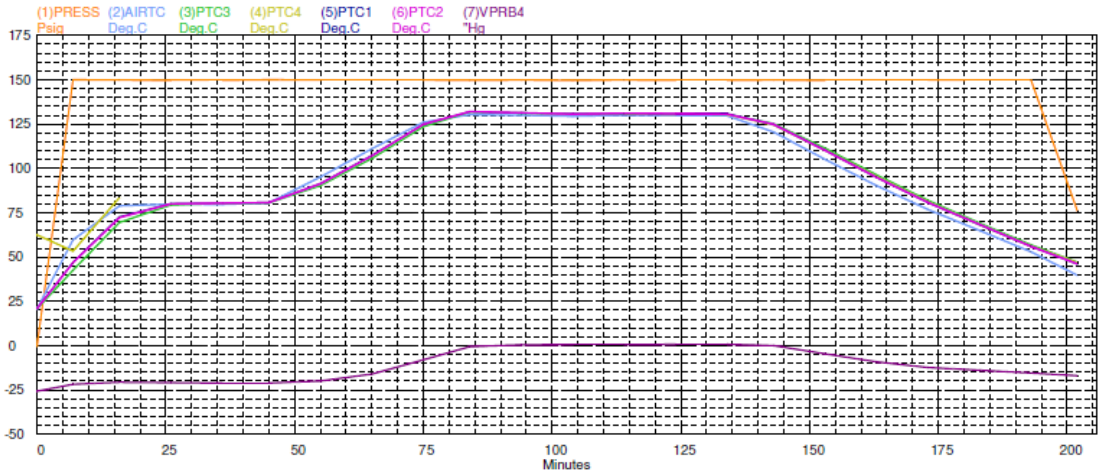

Fig. 5 Variation of temperatures and pressures in the ASC process system over time

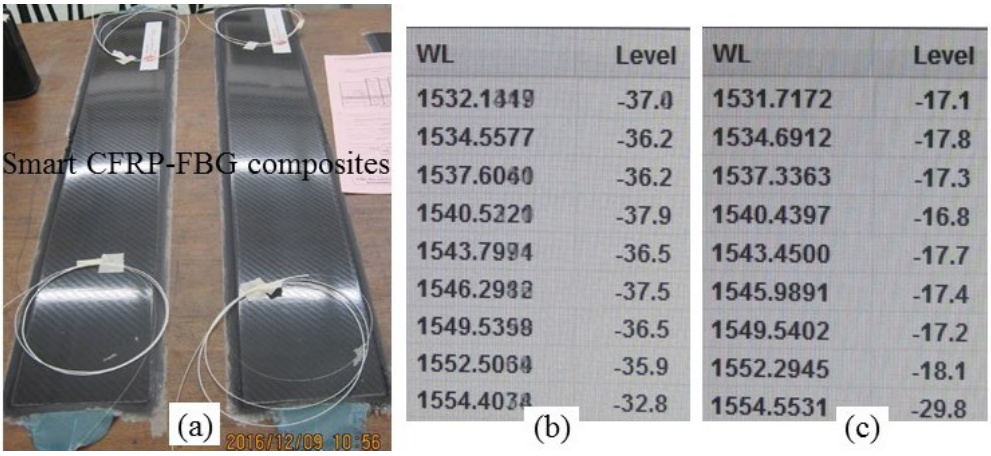

WL	Level
1532.1849	-37.0
1534.5577	-36.2
1537.6060	-36.2
1540.5220	-37.9
1543.7994	-36.5
1546.2982	-37.5
1549.5398	-36.5
1552.5060	-35.9
1554.4034	-32.8

(b)

WL	Level
1531.7172	-17.1
1534.6912	-17.8
1537.3363	-17.3
1540.4397	-16.8
1543.4500	-17.7
1545.9891	-17.4
1549.5402	-17.2
1552.2945	-18.1
1554.5531	-29.8

(c)

Fig. 6 Smart CFRP-FBG composites: (a) Two tested samples; (b) Central wavelengths of FBGs in series in Sample 1; and (c) Central wavelengths of FBGs in series in Sample 2

3.2 Nondestructive testing

The embedment of FBGs in series may induce defects (i.e., micro porosity and microcracks around the embedded optical fiber) in the multi-layer CFRP laminates. For this reason, ultrasonic flaw detector produced by SONATEST is adopted to inspect the inner bonding state of the carbon fiber strips, epoxy resin and optical fibers, as shown in Fig. 7. The Sonatest Veo flaw detector is an advanced phased array ultrasonic testing (PAUT) system used to detect the embedded defects. The Veo has an easy-to-view computer-human interface and simple operating control panel, making it more intuitive to quickly identify defects. The flaw detection of this system is based on ultrasonic pulse-echo (PE) inspection with a linear array ultrasonic wheel probe of 64 elements. The probes are normal to the inspection surface in an immersion configuration and water is used as the couplant. The existing defects, including micropores and microcracks will interact and diffract the incident ultrasonic waves and generate echoes by reflection, resulting in the variation of the received ultrasonic amplitude. With careful selection of the amplitude threshold, it is easy to identify the defects from the A-scan signal. The ultrasonic wheel probe is attached to a 2D scanning frame, enabling a scanning scheme on the surface of the CFRP-FBG

composites and forming amplitude C-scans of this specimen.

The color of C-scans indicates the existence of defects and the deeper color corresponds to the sever defects. The testing results show that the carbon fiber strips have been uniformly distributed and the inserted sensing fiber causes no micro flaws in the CFRP composite. However, small defects exist at the two ends of the CFRP composite, which are caused by the perturbation of white optical fiber loose sleeve. Further measure can be considered to improve the structural integrity of the CFRP composite.

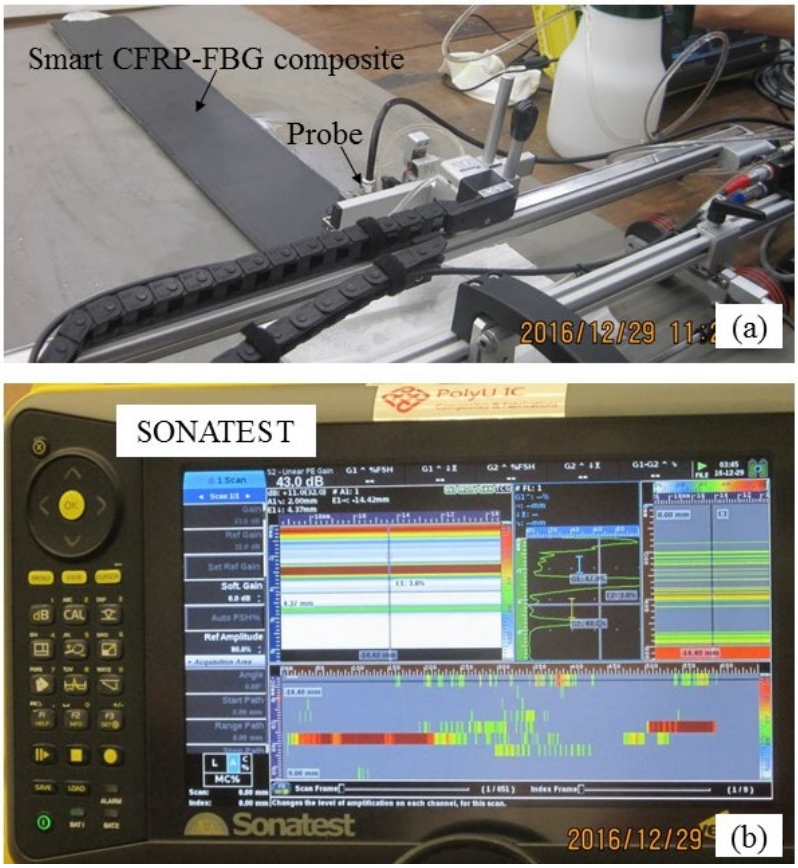

Fig. 7 Ultrasonic testing on the CFRP-FBG composite: (a) Ultrasonic probe; (b) Flaw detector

4. Experimental investigation

4.1 Experimental setup

To examine the measurement accuracy and the possibility of the smart CFRP-FBG composites to perceive the interfacial bonding state, a smart CFRP-FBG composite reinforced steel beam has been designed. As shown in Fig. 8, the span of the steel beam is 1800 mm, and the height and width are both 125 mm. The web width of the H-shaped cross section is 6 mm and the flange thickness is 9 mm. The four-point bending loading mode is designed and the distance between the two loading points is 300 mm. The sensor layout on the CFRP-FBG composite is displayed in Fig. 9. The FBG sensing elements in the plate are numbered as FBGs-e*n* (*n* = 1, 2, 3, …, 9). FBGs-e1 located at the right side has the smallest wavelength (about 1532 nm) and FBGs-e9 located at the left side has the largest

wavelength (1554 nm). The wavelength interval between the two adjacent FBGs is about 3 nm. The distance interval between two adjacent FBGs is about 75 mm. Besides the embedded FBGs, five bare FBGs for proofreading have been bonded on the bottom surface of the composite with fixed intervals (150 mm). The surface-attached FBG sensors are marked as FBG-s*n* (*n* = 1, 2, 3, …5). The smart CFRP-FBG composite developed in Section 3 is attached on the beam bottom with a kind of epoxy resin, as shown in Fig. 10(a). Simply supported constraint is considered and step load is applied to the beam, with its range from 5 kN to 120 kN. The physical model of the reinforced steel beam is displayed in Fig. 10. The data acquisition system Si255 produced by Micro Optic In. is employed to record the data automatically. LVDTs have been installed on the supports and the center to measure the vertical deflection.

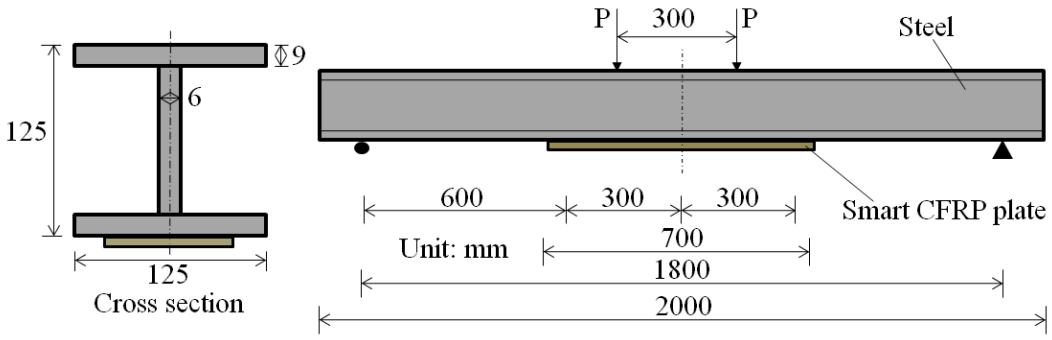

Fig. 8 Configuration of the steel beam reinforced with smart CFRP-FBG composite

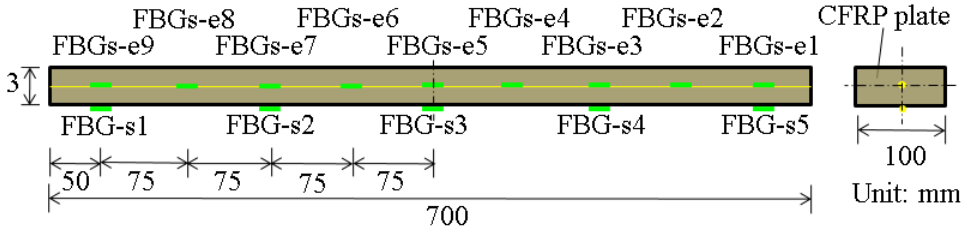

Fig. 9 Layout of sensors on the smart CFRP-FBG composite

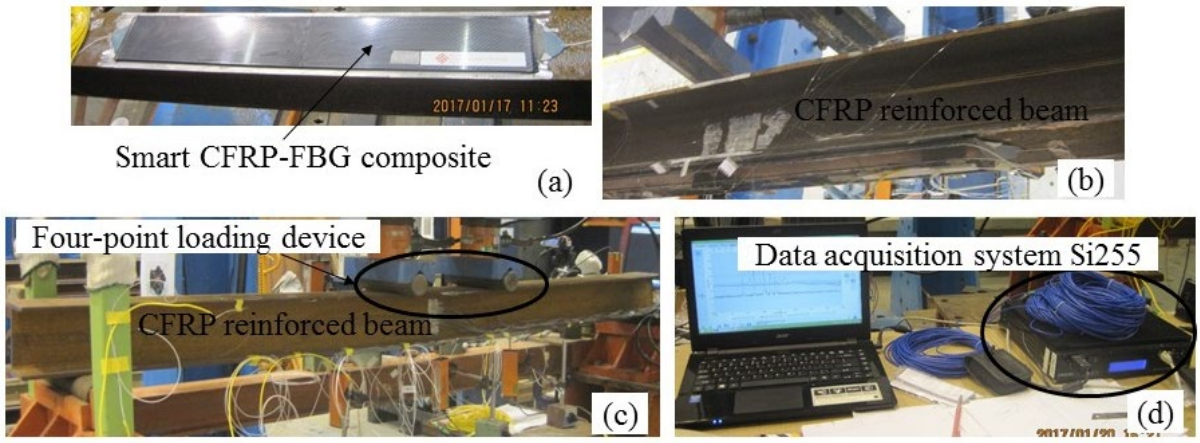

Fig. 10 Physical model in test: (a) Attached CFRP-FBG composite; (b) Reinforced steel beam; (c) Loading setup; (d) Si255 for data acquisition

4.2 Result and discussion

The load-deflection curve in Fig. 11 shows that the CFRP reinforced beam has experienced a relatively long elastic stage. When the load ($2P$) reaches 100 kN, the beam begins to yield. To verify the effectiveness of the developed CFRP-FBG composite for strain measurement, a comparison between the data measured by FBGs in series in the composite and the surface-attached FBGs has been conducted. Fig. 12(a) and Fig. 12(b) separately present the strain profiles under loading ($2P$=5 kN ~ 80 kN). It is shown that the strain profiles experience a stable ascendency with the increase of applied load. The strains measured by FBG sensing elements inside and on the CFRP composite are nearly equivalent. It can be explained that the thickness of the CFRP composite is very thin and the discrepancy is mainly induced by the location difference as manifested in the beam theory. The deformation of the beam at the left side is relatively higher than that at the right side, which can be attributed to the load unequally distributed to the two loading points. In general, the FBGs in the CFRP composite can well reflect the strain state, which implies that the smart CFRP-FBG composite can be instead of additional sensors. The CFRP composite behaves as the protective coating and the sensing fiber contacts directly with the host material (CFRP composite). The strain transfer loss in this case can be avoided, and the strain reading from the FBGs can represent the actual strain of the host material. Besides, the stable increase of the strain profiles with the load along the bonded length also indicates that the deformation of the beam has been well transferred to the CFRP composite, and no interfacial defect occurs during this stage.

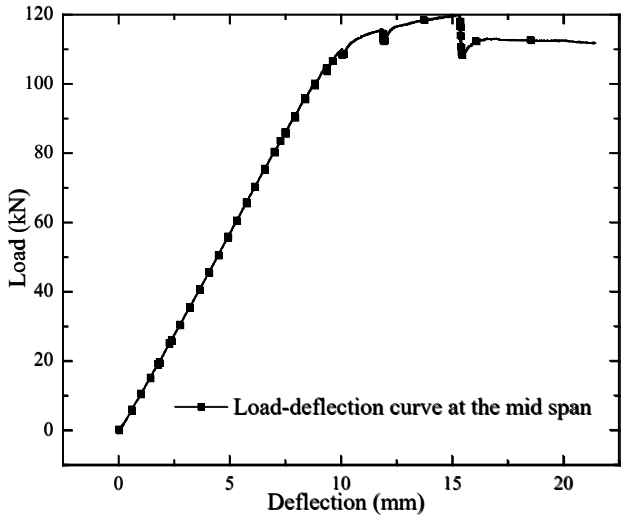

Fig. 11 Load-deflection curve of the CFRP reinforced steel beam at mid-span

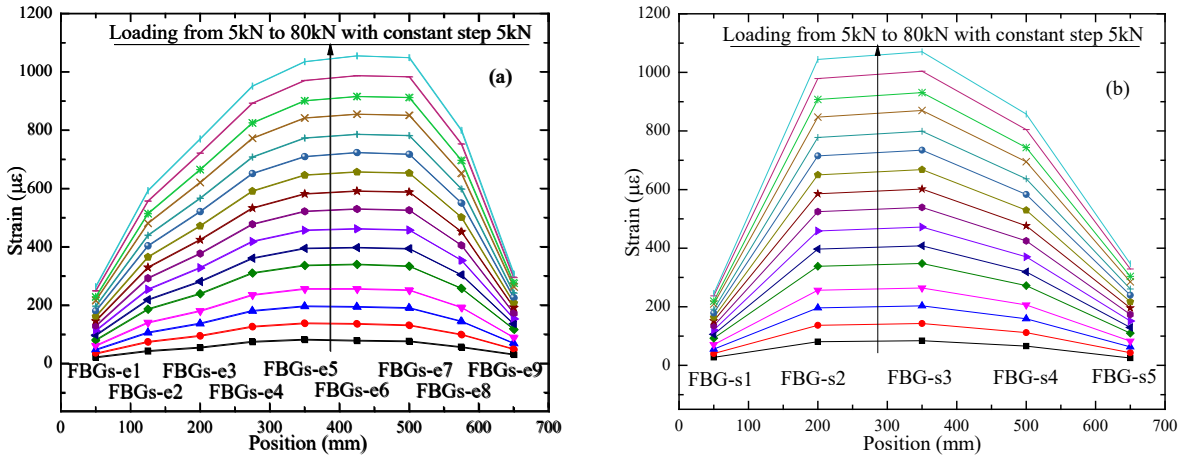

Fig. 12 Strain of the CFRP composite: (a) FBGs in series; (b) FBGs on the bottom surface

4.3 Validation of the proposed method to detect the interfacial bonding state

Considerable research has been conducted to depict the interfacial bonding state. Various principles have been proposed to reflect the bond-slip relationship based on the theoretical analysis and experimental investigation under different loading conditions [62]. The theoretical study presented in Section 2 shows that the interfacial shear stress has close relationship with the normal stress of the CFRP composite under specified assumptions. In other words, it can be adopted to monitor the normal stress (or strain) of the CFRP composite, and then the real-time interfacial bonding state can be identified by using the obtained theoretical function [63]. A comparison between the theoretical results and the measured results is made for the validation of the proposed method. The strain data obtained from the theoretical analysis and those by the monitoring technique under different loads are displayed in Fig. 13. It can be found that the measured strain profiles present a similar evolution pattern with the theoretical strain profiles. The gap between the measured strain curves and the theoretical ones can be attributed to the simplification made in the theoretical analysis, the imperfect interfacial bonding state even in the elastic stage, and the measurement error induced by strain transfer loss [64]. The difference between the theoretical strain and measured strain increases with the increment of the load. This is because the higher load leads to larger discrepancy between the theoretical model and the actual structure. However, the interfacial debonding detection is determined by the continuous strain profiles measured by the FBGs in series, and thus the difference cannot affect the damage identification.

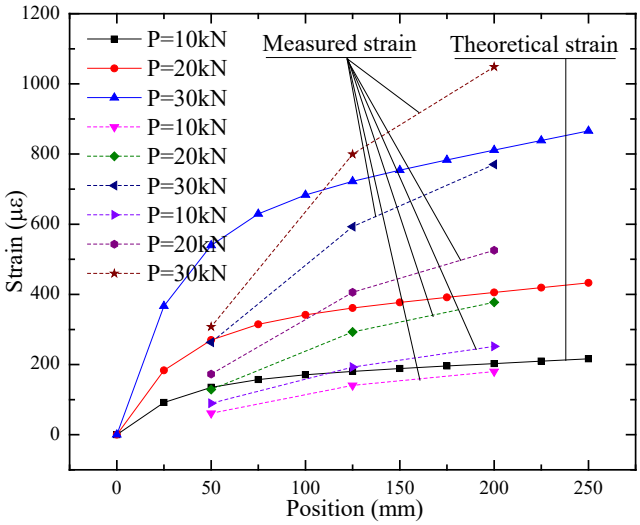

Fig. 13 Predicted strains and measured strains by FBGs in series along the bonded length under different loads

5. Interfacial debonding detection by the smart CFRP-FBG composite

The theoretical analysis in Section 2 shows that the interfacial shear stress between the steel beam and the surface-attached CFRP composite can be described by the normal stress of the CFRP composite. Although the formulated relationship is in the elastic stage, it can still be expected that the interfacial bonding state can be reflected from the evolution of the normal stress (or strain) profiles of the CFRP composite during the whole process. This is because the deformation of the steel beam under different loads is transferred to the CFRP composite by the interfacial bonding stresses. If the interface experiences a gradual deterioration, the load transfer path changes and abnormal variation can be observed in the stress (or strain) profiles of the CFRP composite. The interfacial defect would lead to the deformation transfer loss.

A case study on the tested CFRP reinforced beam is conducted and some conclusions can be drawn from the data analysis. The interfacial debonding failure occurs in the plastic stage at a brittle manner. It starts from one end of the CFRP composite and stops at the axisymmetric center of the reinforced beam, as shown in Fig. 14. The strain profiles measured by the five FBGs attached on the bottom surface of the CFRP composite are presented in Fig. 15. The strain profiles of the FBGs embedded in series into the CFRP composite are illustrated in Fig. 16. It can be seen that the strains go through a linear and stable increase with the increment of load (0-100 kN) in 3000 seconds. During the period of 3000 seconds to 7750 seconds, the strain profiles experience a nonlinear and smooth ascendency with the increase of load (100 kN-120 kN), which means that local defects exist in the system. When the load stabilizes at 120 kN and the corresponding time is around 7750 seconds, sudden changes have been observed in all the strain profiles. It means that the end debonding failure occurs at the 7750 seconds. An obvious increase and decrease of the two pairs of FBG sensing elements (i.e., FBG-s1 and FBG-s5, FBGs-e1 and FBGs-e9) separately located at the two ends of the CFRP composite can be observed from Fig. 15 and Fig. 16. The strain profiles of FBG-s5 and FBGs-

e1 located at the right side of the composite show an abnormal decrease while those of FBG-s1 and FBGs-e9 located at the left side show a sudden increase. It can be inferred that the interfacial debonding starts from the right side, which agrees well with the observed failure mode. The strain profiles in the middle positions have a sudden increase at the 7750 seconds and then decrease at different attenuation rates. It can also be found that the attenuation rate of the strains approaching the debonding point is faster than that away from the debonding point.

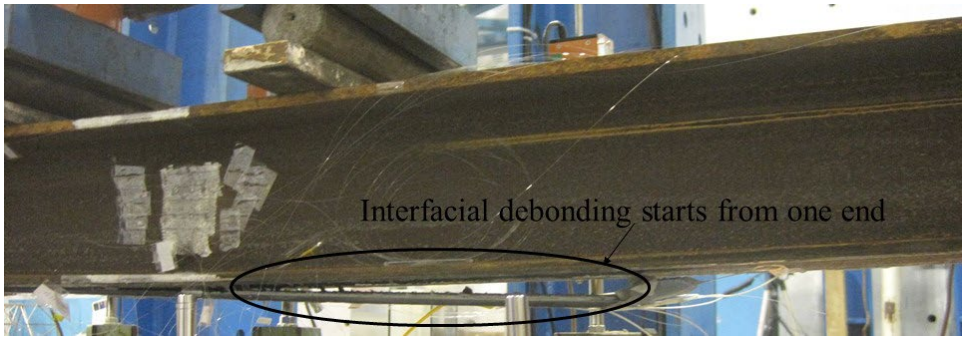

Fig. 14 Interfacial debonding of the smart CFRP-FBG composite strengthened steel beam

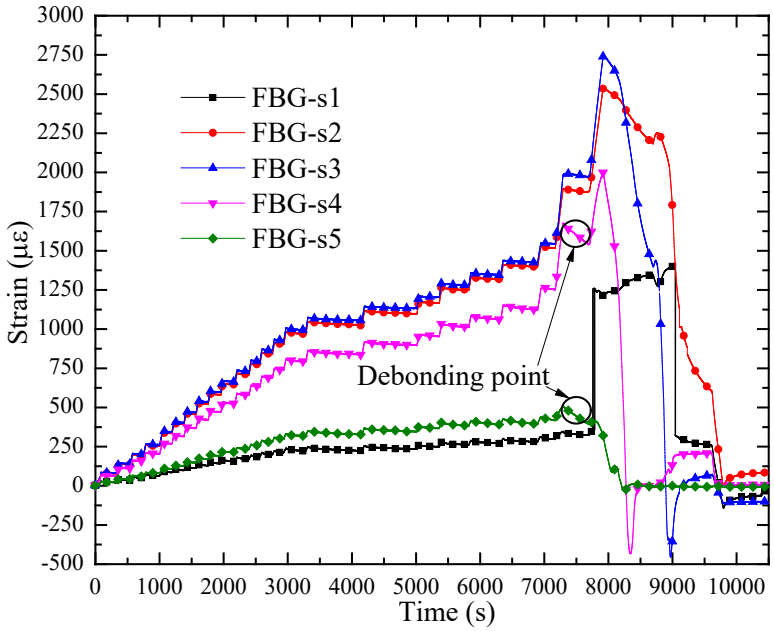

Fig. 15 Strains measured by FBGs attached on the bottom surface of the CFRP composite under increased loads

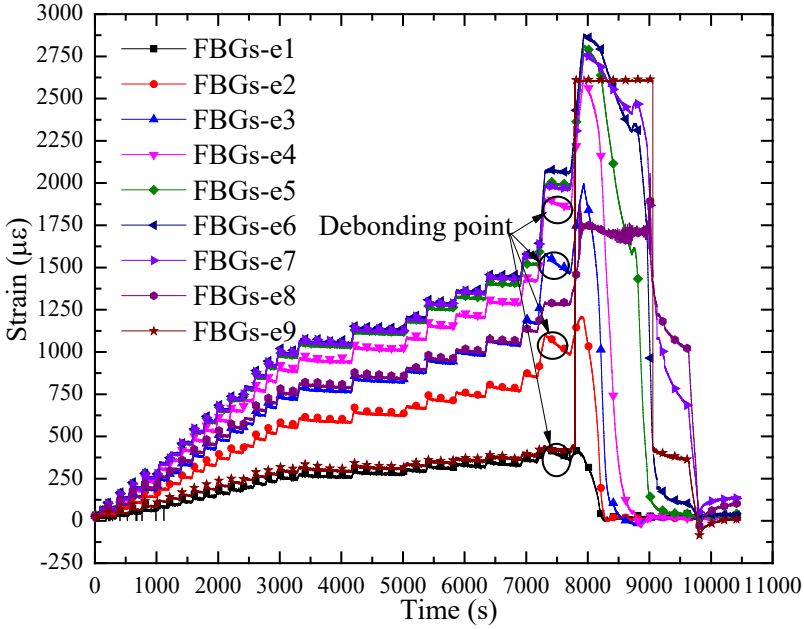

Fig. 16 Strains measured by FBGs in series in the CFRP composite under increased loads

Fig. 17 shows the strain profiles of the CFRP composite measured by FBGs attached on the bottom surface at several different moments. Fig. 18 displays the strain profiles of the composite measured by the embedded FBGs in series. It is seen that local strain has a slight decrease with the occurrence of interfacial debonding under settled load (120 kN). When the interfacial debonding point propagates from the end to the center, the strain profiles present a gradual decadency from the end debonding to the central. The strains at the bond intact zone also decrease and then keep at a very low level. In other words, the interfacial debonding can be identified by inspecting the variation of the continuous strain profiles of the FBGs embedded in series in the CFRP composite.

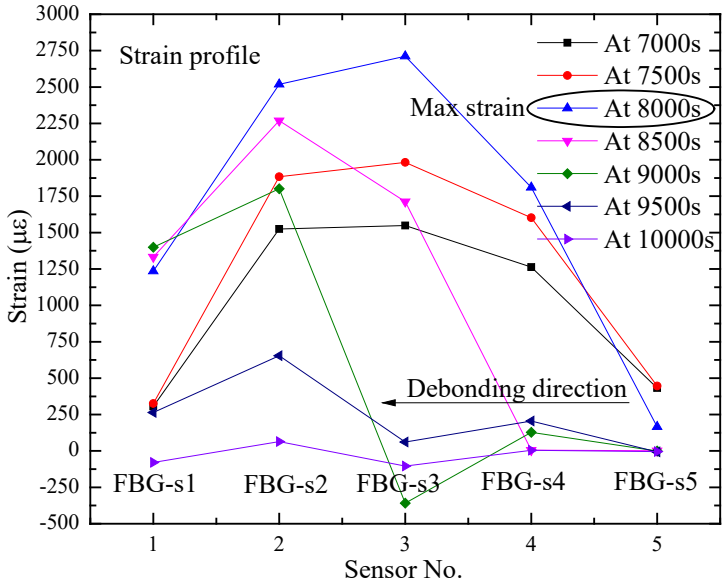

Fig. 17 Variation of strains measured by surface-attached FBGs with the occurrence of interfacial debonding

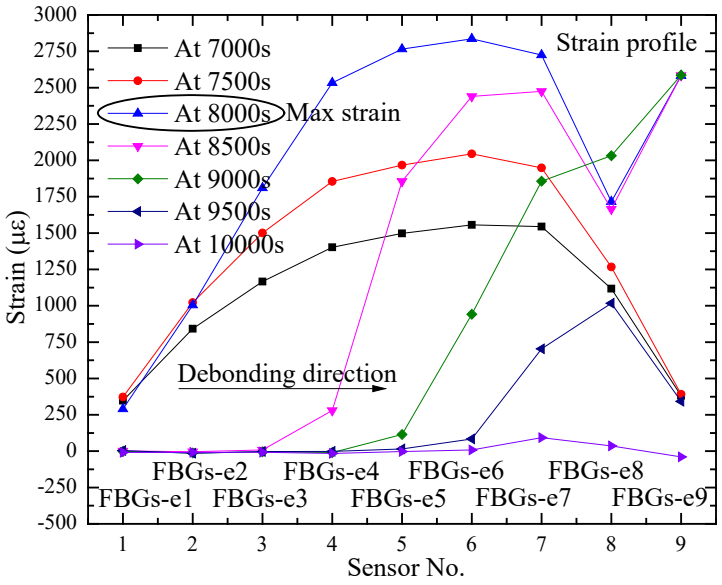

Fig.18 Variation of strains measured by FBGs in series with the occurrence of interfacial debonding

Given the data analysis from Fig. 15 to Fig. 18, it can be concluded that the interfacial debonding can be satisfactorily identified by the strain variation of the smart CFRP-FBG composite in the whole process. The strain profiles measured by the FBGs embedded in series and the surface-attached FBGs of the CFRP composite validate the effectiveness and accuracy of the developed CFRP-FBG composite.

6. Conclusions

To develop a feasible and reliable monitoring technique for identifying the interfacial debonding, a smart CFRP-FBG composite has been designed. Theoretical and experimental investigations have been conducted to verify the effectiveness of the proposed method. The following conclusions can be drawn from the study:

(1) The interaction between the steel beam and the CFRP composite is mainly dependent on the bonding state of the interface, and the interfacial shear stress can be described by the normal stress of the CFRP composite;

(2) The devised CFRP-FBG composite shows a stable structural integrity as corroborated by ultrasonic-based nondestructive testing, and some micro defects induced by the insertion of white optical fiber loose tube exist at the two ends of the CFRP composite;

(3) The FBGs embedded in series in the CFRP composite perform well and provide satisfactory measurement accuracy. In engineering practice, the FBGs embedded in series can substitute for the surface-attached FBG sensors;

(4) The strain profiles of the CFRP composite measured by the FBGs embedded in series and surface-attached FBG sensors validate that the smart CFRP-FBG composite can efficiently identify the

interfacial debonding.

The smart CFRP-FBG composite has been proved to simultaneously strengthen the structure and monitor the interfacial bonding condition. It acts as a novel sensor with multi-function. Study on the damage index extracted from the measurements of the smart CFRP-FBG composite will be conducted in future work, which will be helpful to automatic recognition of the interfacial debonding in an FBG-based SHM system.

Acknowledgements

The work described in this paper was supported by the Research Grants Council of the Hong Kong Special Administrative Region, China (Grant No. T22/502/18), the National Natural Science Foundation of China (Grant No. 51478406 and 51908263), and The Hong Kong Polytechnic University (Grant No. 1-BBAG). The authors would also like to appreciate the funding support by the Innovation and Technology Commission of the Hong Kong SAR Government (Project No. K-BBY1). Special thanks are due to Prof. Jinping Ou and Prof. Zhi Zhou of Dalian University of Technology, and Prof. Youhe Zhou and Prof. Ning Huang of Lanzhou University. The findings and opinions expressed in this article are only those of the authors and do not necessarily reflect the views of the sponsors.

References

[1] Sikdar S., Banerjee S. (2017). Structural health monitoring of advanced composites using guided waves. LAP LAMBERT Academic Publishing, Beau Bassin. ISBN 978-620-2-02697-0.
[2] Carlos T.B., Rodrigues J.P.C., Lima R.C.A., Dhima D. (2018). Experimental analysis on flexural behavior of RC beams strengthened with CFRP laminates and under fire conditions. Composite Structures, 189, 516-528.
[3] Sikdar S., Mirgal P., Banerjee S., Ostachowicz W. (2019). Damage-induced acoustic emission source monitoring in a honeycomb sandwich composite structure. Composites Part B: Engineering, 158, 179-188.
[4] Oehlers D.J., Moran J.P. (1990). Premature failure of externally plated reinforced concrete beams. Journal of Structure Engineering, 116(4), 978-995.
[5] Oehlers D.J. (1992). Reinforced concrete beams with plates glued to their soffits. Journal of Structure Engineering, 118(8), 2023-2038.
[6] Rabinovitch O., Frostig Y. (2001). Nonlinear high-order analysis of cracked RC beams strengthened with FRP strips. Journal of Structure Engineering, 127(4), 381-389.
[7] Saadatmanesh H., Ehsani M.R. (1991). RC beams strengthened with GFRP plates. 1: experimental study. Journal of Structure Engineering, 117(11), 3417-3433.
[8] Taljsten B. (1997). Strengthening of beams by plate bonding. Journal of Materials in Civil Engineering, 9(4), 206-212.
[9] Saadatmanesh H., Malek A.M.(1998). Design guidelines for flexural strengthening of RC beams with FRP plates. Journal of Composites for Construction, 2(4), 158-164.
[10] Swamy R.N., Mukhopadhyaya P. (1999). Dedonding of carbon-fibre-reinforced polymer plate from concrete beams. Proc. Instn Civ. Engrs Structs & Bldgs, 134, 301-317.
[11] Wu Z.S., Niu H.D. (2000). Study on debonding failure load of RC beams strengthened with FRP sheets. Journal of Structure Engineering, 46A, 1431-1441.
[12] Smith S.T., Teng J.G. (2001). Interfacial stresses in plated beams. Engineering Structures, 23, 857-871.
[13] Teng J.G., Zhang J.W., Smith S.T. (2002). Interfacial stresses in reinforced concrete beams bonded with a soffit plate: a finite element study. Construction and Building Materials, 16, 1-14.
[14] Teng J.G., Yuan H., Chen J.F. (2006). FRP-to-concrete interfaces between two adjacent cracks: theoretical model for debonding failure. International Journal of Solids and Structures, 43, 5750-5778.
[15] Sikdar S., Ostachowicz W. (2019). Nondestructive analysis of core-junction and joint-debond effects in advanced composite structure. Polymer Testing, 73, 31-38.
[16] Mukhopadhvava P., Swamy N. (2001). Interface shear stress: a new design criterion for plate debonding. Journal of Composites for Construction, 5(1), 35-43.
[17] Rahimi H., Hutchinson A. (2001). Concrete beams strengthened with externally bonded FRP plates. Journal of Composites for Construction, 5(1), 44-56.

[18] Zhao X.L., Zhang L. (2007). State-of-the-art review on FRP strengthened steel structures. Engineering Structures, 29, 1808-1823.
[19] Teng J.G., Yu T., Fernando D. (2012). Strengthening of steel structures with fiber-reinforced polymer composites. Journal of Constructional Steel Research, 78, 131-143.
[20] Dai J.G., Gao W.Y., Teng J.G. (2013). Bond-slip model for FRP laminates externally bonded to concrete at elevated temperature, Journal of Composites for Construction, 17(2), 217-228.
[21] Korayem A.H., Li C.Y., Zhang Q.H., Zhao X.L., Duan W.H. (2015). Effect of carbon nanotube modified epoxy adhesive on CFRP-to-steel interface. Composites Part B: Engineering, 79, 95-104.
[22] Ou J.P., Li H. (2010). Structural health monitoring in mainland China: review and future trends. Structural Health Monitoring-An International Journal, 9(3), 219-231.
[23] Ou J.P. (2005). Some recent advances of intelligent health monitoring systems for civil infrastructures in HIT. SPIE, Fundamental Problems of Optoelectronics and Microelectronics II, 5851.
[24] Ou J.P. (2005). Research and practice of smart sensor networks and health monitoring systems for civil infrastructures in mainland China. Bulletin of National Science and Foundation of China, 1, 8-12.
[25] Glisic B., Yao Y. (2012). Fiber optic method for health assessment of pipelines subjected to earthquake-induced ground movement. Structural Health Monitoring, 11(6), 696-711.
[26] Luyckx G., Voet E., Lammens N., Degrieck J. (2011). Strain measurements of composite laminates with embedded fibre Bragg gratings: criticism and opportunities for research. Sensors, 11, 384-408.
[27] Ansari F. (2007). Practical implementation of optical fiber sensors in civil structural health monitoring. Journal of Intelligent Material Systems and Structures, 18(8), 879-889.
[28] Luyckx G., Voet E., Waele W.D., Degrieck J. (2010). Multi-axial strain transfer from laminated CFRP composites to embedded Bragg sensor. I. parametric study. Smart Materials and Structures, 19(10), 105017-1-9.
[29] Smith S.T., Teng J.G. (2002). FRP-strengthened RC beams.1: review of debonding strength models. Engineering Structures, 24, 385-395.
[30] Tavakkolizadeh M., Saadatmanesh H. (2003). Repair of damaged steel-concrete composite girders using carbon fiber-reinforced polymer sheets. Journal of Composites for Construction, 7(4), 311-322.
[31] Ceroni F., Ianniciello M., Pecce M. (2016). Bond behavior of FRP carbon plates externally bonded over steel and concrete elements: experimental outcomes and numerical investigations. Composites Part B: Engineering, 92, 434-446.
[32] Calderon P.A., Glisic B. (2012). Influence of mechanical and geometrical properties of embedded long-gauge strain sensors on the accuracy of strain measurement. Measurement Science and Technology, 23(9), 065604.
[33] Wang H.P., Jiang L.Z., Xiang P. (2018). Priority design parameters of industrialized optical fiber sensors in civil engineering. Optics and Laser Technology, 100, 119-128.
[34] Degala S., Rizzo P., Ramanathan K., Harries K.A. (2009). Acoustic emission monitoring of CFRP reinforced concrete slabs. Construction and Building Materials, 23(5), 2016-2026.
[35] Xu B., Zhang T., Song G.B., Gu H.C. (2013). Active interface debonding detection of a concrete-filled steel tube with piezoelectric technologies using wavelet packet analysis. Mechanical Systems and Signal Processing, 36, 7-17.
[36] Sikdar S., Ostachowicz W. (2019). Ultrasonic Lamb wave-based debonding monitoring of advanced honeycomb sandwich composite structures. Strain, 55(1), 1-15.
[37] Sikdar S., Fiborek P., Kudela P., Banerjee S., Ostachowicz W. (2019). Effects of debonding on Lamb wave propagation in a bonded composite structure under variable temperature conditions. Smart Mater. Struct., 28, 015021-1-13.
[38] Xu H., Su Z.Q., Cheng L., Guyader J.L., Hamelin P. (2013). Reconstructing interfacial force distribution for identification of multi-debonding in steel-reinforced concrete structures using noncontact laser vibrometry. Structural Health Monitoring, 12(5-6), 507-521.
[39] Hong S.D., Harichandran R.S. (2005). Sensors to monitor CFRP/concrete bond in beams using electrochemical impedance spectroscopy. Journal of Composites for Construction, 9(6), 515-523.
[40] Sohn H., Kim S.D., In C.W., Cronin K.E. (2008). Debonding monitoring of CFRP strengthened RC beams using active sensing and infrared imaging. Smart Structures and Systems, 4(4), 391-406.
[41] Ansari F. (2007). Practical implement of optical fiber sensors in civil structural health monitoring of bridges. Journal of Intelligent Materials, Systems and Structures, 18(8), 879-889.
[42] Glisic B. (2011). Influence of the gauge length on the accuracy of long-gauge sensors employed in monitoring of prismatic beams. Measurement Science and Technology, 22, 035206.
[43] Xu Y., Leung C.K. Y., Tong P., Yi J., Lee S.K.L. (2005). Interfacial debonding detection in bonded repair with a fiber optical interferometric sensor. Composites Science and Technology, 65(9), 1428-1435.
[44] Wang H.P., Xiang P., Li X. (2016). Theoretical analysis on strain transfer error of FBG sensors attached on steel structures subjected to fatigue load. Strain, 52(6), 522-530.
[45] Wang H.P., Jiang L.Z., Xiang P. (2018). Improve the durability of the optical fiber sensor based on strain

transfer analysis. Optical Fiber Technology, 42, 97-104.
[46] Wang H.P., Xiang P., Jiang L. Z. (2019). Strain transfer theory of industrialized optical fiber-based sensors in civil engineering: a review on measurement accuracy, design and calibration. Sensors & Actuators: A. Physical, 285, 414-426.
[47] Yin X., Huang N., Wang Z.S. (2017). A numerical investigation into sand grain/slope bed collision. Powder Technology, 314, 28-38.
[48] Huang N., Shi G.L. (2017). The significance of vertical moisture diffusion on drifting snow sublimation near snow surface. The Cryosphere, 11, 3011-3021.
[49] Liu B. X., Jing Z., Yong H.D., Zhou Y.H. (2017). Strain distributions in superconducting strands with twisted filaments. Composite Structures, 174, 158-165.
[50] Wang J.Q., Liu X.J., Zhou Y.H. (2018). A high-order accurate wavelet method for solving Schrodinger equations with general nonlinearity. Applied Mathematics and Mechanics (English Edition), 39(2), 275-290.
[51] Zhao Y., Ansari F. (2002). Embedded fiber optic sensor for characterization of interface strains in FRP composite. Sensors and Actuators A, 100, 247-251.
[52] Ansari F. (2005). Fiber optic health monitoring of civil structures using long gage and acoustic sensors. Smart Materials and Structures, 14(3), S1-S7.
[53] Takeda S., Okabe Y., Yamamoto T., Takeda N. (2003). Detection of edge delamination in CFRP laminates under cyclic loading using small-diameter FBG sensors. Composites Science and Technology, 63, 1885-1894.
[54] Mizutani T., Okabe Y., Takeda N. (2003). Quantitative evaluation of transverse cracks in carbon fiber reinforced plastic quasi-isotropic laminates with embedded small-diameter fiber Bragg grating sensors. Smart Materials and Structures, 12, 898-903.
[55] Takeda S., Aoki Y., Nagao Y. (2012). Damage monitoring of CFRP stiffened panels under compressive load using FBG sensors. Composite Structures, 94, 813-819.
[56] Lammmens N., Luyckx G., Voet E., Paepegem W.V., Degrieck J. (2015). Optimization of coating diameter of fiber optic sensors embedded in composite structures under arbitrary loading conditions. Smart Materials and Structures, 24, 115003-1-12.
[57] Bastianini F., Corradi M., Borri A., di Tommaso A. (2005). Retrofit and monitoring of an historical building using “Smart” CFRP with embedded fibre optic Brillouin sensors. Construction and Building Materials, 19, 525-535.
[58] Lu S.W., Xie H.Q. (2007). Strengthen and real-time monitoring of RC beam using “intelligent” CFRP with embedded FBG sensors. Construction and Building Materials, 21, 1839-1845.
[59] Kerrouche A., Boyle W.J.O., Gebremichael Y., Sun T., Grattan K.T.V., Taljsten B., Bennitz A. (2008). Field tests of fibre Bragg grating sensors incorporated into CFRP for railway bridge strengthening condition monitoring. Sensors and Actuators A: Physical, 148, 68-74.
[60] Jiang G.L., Dawood M., Peters K., Rizkalla S. (2010). Global and local fiber optic sensors for health monitoring of civil engineering infrastructure retrofit with FRP materials. Structural Health Monitoring, 9(4), 309-322.
[61] Wang C., Cheng L.J. (2014). Use of fiber Bragg grating sensors for monitoring concrete structures with prestressed near-surface mounted carbon fiber–reinforced polymer strips. Journal of Intelligent Material Systems and Structures, 25(2), 164-173. https://doi.org/10.1177/1045389X13489364
[62] Taljsten B. (1997). Strengthening of beams by plate bonding. Journal of Materials and Civil Engineering, 9(4), 206-212.
[63] Gao W.Y., Dai J.G., Teng J.G. (2015). Analysis of mode II debonding behavior of fiber-reinforced polymer-to-substrate bonded joints subjected to combined thermal and mechanical Loading. Eng. Fract. Mech. 136, 241-264.
[64] Wang H.P., Dai J.G. (2019). Strain transfer analysis of fiber Bragg grating sensor assembled composite structures subjected to thermal loading. Composites Part B: Engineering, 162, 303-313.